A large-eddy simulation study on vortex-ring collisions upon round cylinders

T. H. New*, G. J. Gotama[†] and U S Vevek[††]

School of Mechanical and Aerospace Engineering, Nanyang Technological University

50 Nanyang Avenue, Singapore 639798

Abstract

A large-eddy simulation based numerical study was conducted on head-on collisions between vortex-rings and round cylinders. The vortex-ring Reynolds number was Re=4000, while the ratio of cylinder diameter to vortex-ring diameter (i.e. diameter ratio, D/d) was varied from 4 to 1. Vortical behaviour predicted by the present simulations are observed to agree well with an earlier experimental study [*T. H. New and B. Zang, Journal of Fluid Mechanics, volume 833, page 648 (2017)*]. Present simulations also reveal additional flow details on the vortex dynamics and vortex-core trajectories which have not been observed previously. Firstly, vortex-dipoles produced by D/d $\leqslant$2 cylinders are cross-sections of elliptic vortex-ringlets formed via vortex disconnection/ reconnection of secondary vortex-ring segments. Secondly, the aspect ratio of the elliptic vortex-ringlets increases when a smaller diameter-ratio cylinder is used and finally, they undergo axis-switching behaviour. Furthermore, up to three sets of tertiary vortex-ring cores are formed along the D/d=2 and 1 cylinder straight-edges, where they subsequently merge with the secondary vortex-ring cores within the confines of the primary vortex-ring cores. This merged vortex core moves towards the collision axis and forms an inner vortex-dipole with a wall separated vortex. Along the convex surface, up to two sets of tertiary vortex-ring cores are observed for D/d=2 and 1 cylinders and trajectories of the vortex-dipoles agree well with the past experimental results. These observations support the notion that higher vortex-stretching levels resulting from the use of small diameter-ratio cylinders with higher surface curvatures underpin the wide range of vortical behaviour observed here.

Keywords: vortex ring; collision; cylinder; numerical simulation; large-eddy simulation

* Corresponding author – dthnew@ntu.edu.sg

† Present address – Department of Mechanical Engineering, University of Melbourne, Grattan Street, Parkville, Victoria 3010, Australia

†† Present address – School of Engineering, University of Liverpool, Brownlow Hill, Liverpool L69 3GH, United Kingdom

1. Introduction

Incompressible vortex-rings colliding with rigid, solid boundaries have been of significant fundamental interest among fluid dynamists, due to the myriad of vortex structures produced during the collision process. The collision flow phenomenon and resulting vortex structures play not only an important role in our collective understanding of the details of vortex-boundary layer and vortex-vortex interactions, they also offer insights into optimizing jet-impingement based heat transfer applications. In most applications, the primary geometry of concern is flat and hence it should not come as a surprise that most previous research work concentrated on vortex-ring collisions upon flat surfaces either normally or at some inclined angle. These studies will include but not limited to those conducted by Walker et al. (1987), Lim (1989), Lim et al. (1991), Orlandi and Verzicco (1993), Verzicco and Orlandi (1994), Swearingen et al. (1995), Chu et al. (1995), Fabris et al. (1996), Naitoh et al. (2001), Cheng et al. (2010), Couch and Krueger (2011), New et al. (2016, 2020), Sun and Brücker (2017), spanning a period of almost four decades.

However, vortex-ring collisions upon other solid boundary types had garnered increasing interest as well. Take for instance, Adhikari and Lim (2009), Hrynuk et al. (2012), Naaktgeboren et al. (2012), Cheng et al. (2014), Musta and Krueger (2014), Mujal-Colilles et al. (2015), Hrynuk et al. (2018), Xu et al. (2019, 2021) and Li et al. (2020) had recently investigated how various porous screen parameters affect the collision process. It is most interesting to note that Adhikari and Lim (2009) observed that a new vortex-ring could form downstream of the screen from flow reorganizations after a sufficiently high Reynolds number vortex-ring had collided with it. In addition, other less

conventional collision scenarios have also been pursued by Hu and Peterson (2018, 2021), where they experimentally investigated the outcomes arising from a vortex-ring colliding with a circular aperture coaxially. Their results show that the aperture-to-ring radius ratio plays a key role in determining the behaviour of the collision process, especially with respect to how much of the primary vortex-ring will be blocked or if a new vortex-ring will be formed downstream of the aperture with partial blockage. In addition, Li and Bruecker (2018) investigated vortex-rings colliding with surfaces with protruding slender circular posts and observed flow transitional differences between random and hexagonal post arrangements. Posts arranged randomly did not have appreciable coherent impact upon the vortex-ring after the collision, while the hexagonally arranged posts led to faster growths in the secondary vortex structures and eventual formation of six distinct lobes. Of particular interest, radial jets were detected at the outer tips of the six lobes and implied that near-wall mixing could be enhanced.

In contrast, vortex-ring collisions upon round solid boundaries such as spheres, convex/concave walls or round cylinders have received significantly less attention as the above vortex-ring collision configurations. Nguyen et al. (2019) conducted both experiments and simulations on vortex-ring collisions upon a round sphere, where the sphere diameter was 3 times the orifice size. The effects of lateral offset between the vortex-ring and sphere were investigated as well and results showed that coaxial collisions are relatively two-dimensional, while non-coaxial collisions led to nonuniform circulation of the primary vortex-ring and more three-dimensional resulting flow structures and behaviour. Ahmed and Erath (2020) reported upon an experimental investigation on vortex-ring collision upon hemispherical concave wall, where the ratio of vortex-ring diameter to that of the concave wall ranged from 0.25 to 0.67. Their PIV measurements revealed three different flow outcomes observed, depending on the above-mentioned ratio. For relatively large concave walls, secondary vortex-rings that move towards the collision axis are formed after the primary vortex-ring collides with the concave wall. Subsequently, the secondary vortex-ring cores meet at the collision

axis and move towards the upstream direction. For smaller concave walls, the primary vortex-ring will begin to interact significantly with the wall lip, though the behaviour of the secondary vortex-ring remains relatively similar to that for larger concave walls.

Earlier studies by Naitoh et al. (1995), Ren et al. (2015) and New and Zang (2017) had also shed some light on the most important differences in the flow characteristics between flat-surface and round-cylinder based vortex-ring collisions, many aspects with respect to the changes to the vortex dynamics when the cylinder surface curvature varies remain unknown. Naitoh et al. (1995) conducted one of the earliest and most systematic studies on such a flow scenario, making use of round cylinders with diameter-ratios (i.e. ratio of cylinder diameter, D, to orifice/nozzle diameter, d) of D/d=0.00125 to 0.15. The study not only revealed that additional secondary vortices will be produced when the primary vortex-ring collides with a cylinder that possesses diameter-ratios past a critical value, the primary vortex-ring will also undergo changes to its original circular shape ranging from hexagonal to diamond shape. As for Ren et al. (2015), their large-eddy simulation (LES) revealed for the first time the three-dimensional flow intricacies that accompanied vortex-ring collisions upon round cylinders where the cylinder diameter is comparable to the vortex ring diameter (i.e. D/d=0.5). Motivated by these studies, New and Zang (2017) conducted an experimental study to investigate the vortex dynamics of similar vortex-ring collisions but with diameter-ratios ranging from 1 to 4. Their results demonstrated high sensitivity of the vortex dynamics towards the diameter-ratio, where the former can differ substantially once the latter varies.

While the flow visualization and measurement results from New and Zang (2017) reveal the most important changes in the large-scale vortex dynamics as the diameter-ratio varies, production and behaviour of smaller-scale vortex structures arising from the interactions between the larger-scale ones are not as clear. This is due to the use of 2D laser-induced fluorescence and time-resolved

particle-image velocimetry in that study, which inevitably led to challenges in providing the most accurate 3D flow interpretations possible. In particular, the exact mechanisms responsible for the production of the vortex-dipoles and vortex-ringlets, as well as their different trajectories when different diameter-ratios were used, observed in that study need additional investigation. These are not only intriguing flow features and phenomena, but also could potentially provide further clarity on how heat transfer levels may be improved. Understanding these flow features through further investigations will shed more light on such a collision scenario and bring more clarity to just how different are vortex-ring collisions with flat surfaces and round cylinders as well. This is especially important when the interactions between the primary and secondary vortex-rings and formation of vortex-ringlets are highly dynamical and transient as observed by New and Zang (2017). Motivated by these considerations, OpenFOAM based LES were utilized to study vortex-ring collisions with round cylinders under relatively similar conditions as those used by the earlier experimental study. The availability of transient flow results from these numerical simulations will not only address some of the interpretational uncertainties associated with the previous experimental endeavour, but it will also provide more complete understanding of the vortex-ring collision behaviour.

2. Numerical setup and procedures

All simulations were based on Large-Eddy Simulation (LES) approach and conducted using OpenFOAM® V5. The filtered, incompressible Navier-Stokes equations are given by,

$$\nabla \cdot \overline{\boldsymbol{u}} = 0, \tag{1}$$

$$\partial_t \overline{\boldsymbol{u}} + \nabla \cdot (\overline{\boldsymbol{u}}\,\overline{\boldsymbol{u}}) = -\nabla \overline{P} + \nabla \cdot \left[\left(\nu + \nu_{sgs}\right)(\nabla \overline{\boldsymbol{u}} + (\nabla \overline{\boldsymbol{u}})^{\mathrm{T}})\right], \tag{2}$$

where $P = (p-p_0)/\rho_0$. The transient, incompressible flow solver *pimpleFoam* solves these equations using a combination of PISO (Issa, 1986) and SIMPLE (Patankar, 2018) algorithms. The solver was modified by omitting a flux correction term to reduce the numerical dissipation (Vuorinen et al., 2014). The kinematic viscosity was set to $\nu=10^{-6}m/s^2$ while the eddy viscosity, ν_{sgs}, which accounts for the unresolved sub-grid scales (SGS), was computed using the Smagorinsky model (Smagorinsky,

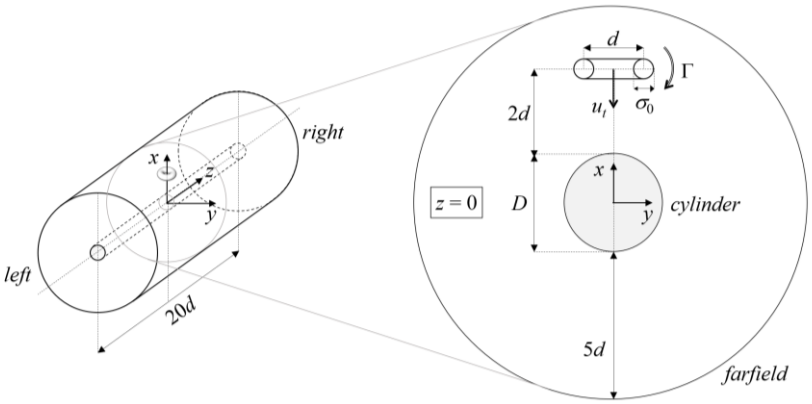

Fig. 1 Schematics of computational domain and initial problem configuration (not drawn to scale).

1963). Linear schemes were used for spatial discretization and a blended Euler/Crank-Nicolson scheme was used for time marching. The computation domain and the initial problem configuration at the z=0 plane are shown in Figure 1. The cylinder and vortex-ring core-to-core diameters are denoted by D and d, respectively, and the computational domain extends from -10d to 10d in the z-direction. Regardless of the exact cylinder diameter, the far-field boundary is always located 5d away from the cylinder surface and hence, the computational domain size increases radially with the cylinder diameter. The cylinder surface was modelled as a "non-slip" wall while Neumann boundary conditions were applied at the far-field boundary. The left and right boundaries were set to be periodic.

The vortex-rings in the experiments by New and Zang (2017) were produced by ejecting a "cylindrical water slug" out of a round nozzle by driving a piston at various pre-defined velocities and therefore, Reynolds numbers. To model after the experimental conditions in general while keeping certain aspects idealized, the vortex-ring core-to-core diameter here was fixed at d=20mm to match the nozzle inner diameter used in the past experiments. Furthermore, the initial translational velocity of the vortex-ring was set to u_t=20mm/s (in the negative x-direction) based on the maximum velocity of the driving piston. Representing u_t by the following expression (Lamb, 1993),

$$u_t = \frac{\Gamma}{2\pi d}\left(\ln\frac{4d}{\sigma_0} - \frac{1}{4}\right) \quad (3)$$

the initial circulation strength, Γ, could be determined. Subsequently, the velocity field was initialized using this initial circulation strength according to the formulation adopted successfully by Cheng et al. (2010) in their vortex-ring simulations,

$$\overline{\boldsymbol{u}}(\boldsymbol{\sigma}, 0) = \frac{\Gamma}{2\pi\|\boldsymbol{\sigma}\|^2}\left[1 - e^{-(\|\boldsymbol{\sigma}\|/\sigma_0)^2}\right]\left(\boldsymbol{\sigma} \times \left(-\widehat{\boldsymbol{k}}\right)\right) \quad (4)$$

where $\boldsymbol{\sigma}$ denotes the radial vector from the vortex core and $\widehat{\boldsymbol{k}}$ denotes the unit vector in the z-direction. The vortex-ring was initialized at a distance of 2d upstream of the round cylinder surface at x=2d + 0.5D, as earlier experimental results show that the vortex-rings are not discernibly perturbed by the presence of the round cylinder based on that separation distance upstream of the round cylinders.

Simulations were conducted for three different round cylinders with diameter-ratios of D/d=1, 2 and 4. For each configuration, the domain was discretized using a 172 × 688 × 172 structured mesh (i.e., 172 cells in the azimuthal direction, 688 cells in the radial direction and 172 cells in the spanwise (z) direction). Since the computational domain size increases radially with the round cylinder diameter, the resolution varies between the three round cylinders in the azimuthal direction. In particular, the smallest cell size in the azimuthal direction for D/d=1, 2 and 4 round cylinders measure 9.13×10^{-5}m, 1.83×10^{-4}m and 3.65×10^{-4}m respectively. On the other hand, since the computational domain span remains constant throughout and far-field boundary is always at 5d away from the cylinder surfaces for all cases, the smallest cell sizes in the spanwise and radial directions are maintained at 7.69×10^{-4}m and 4.88×10^{-5}m respectively. Based on a vortex-ring Reynolds number of $Re=u_t d/\nu=4000$ which is used in the present study, the non-dimensional wall-normal spacing was designed such that $\Delta r^+\approx1$ with nine cells within $0 < r^+ < 10$. Additionally, the non-dimensional near-wall spacings in the azimuthal and spanwise directions were kept at 6 and 13, respectively – well below the recommended spacings for high-resolution LES (Jiang and Lai, 2016). Each simulation was

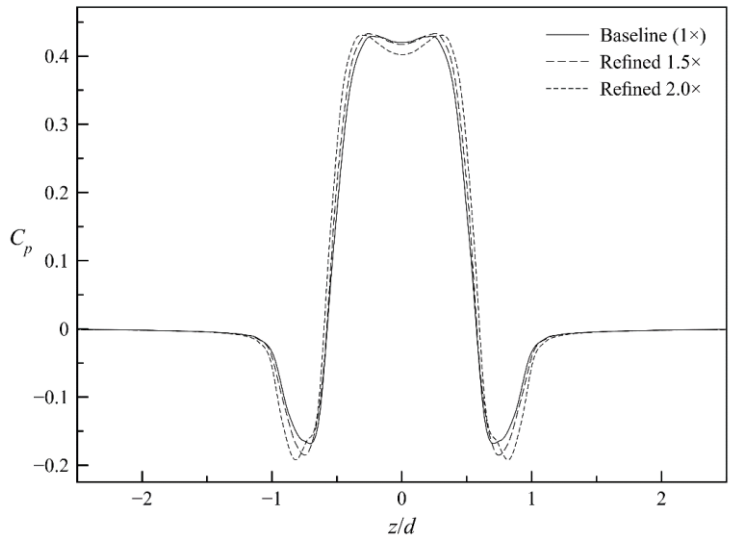

Fig. 2 Comparison of pressure coefficient along the upper surface of the D/d=4 cylinder at τ=2.4 for all three different mesh resolutions.

performed using parallel computations with 96 processors until a non-dimensional time of $\tau=tu_t/d=14$ with a maximum Courant-Friedrichs-Lewy (CFL) condition of unity.

To evaluate if the mesh resolution adopted for the present simulations was satisfactory, D/d=4 round cylinder based vortex-ring collisions were further simulated using two finer 197 × 788 × 197 and 217 × 868 × 217 structured meshes. Note that these two finer meshes have 1.5 and 2 times the number of cells as the baseline mesh (i.e. 172 × 688 × 172) described earlier. Note that these validation simulations were performed up to τ=12. For a more rigorous mesh validation, the pressure fields along a line along the upper surface of the D/d=4 round cylinder in the z-direction (i.e. passing through the point (D/2, 0)) for all three mesh resolutions were extracted at a time after the primary vortex-ring had already collided with the round cylinder with secondary and tertiary vortex-rings undergoing developments and interacting with the primary vortex-ring. In this case, a timing of τ=2.4 was selected and the pressure coefficient, $C_p=(d/\Gamma)^2P$, results are shown in Fig. 2. It can be seen from the comparison that 50% and 100% increases in the mesh resolution (i.e. termed as refined 1.5X and 2.0X configurations in the figure) do not lead to significant differences in the pressure coefficient distributions, while incurring significant increases in the computational times.

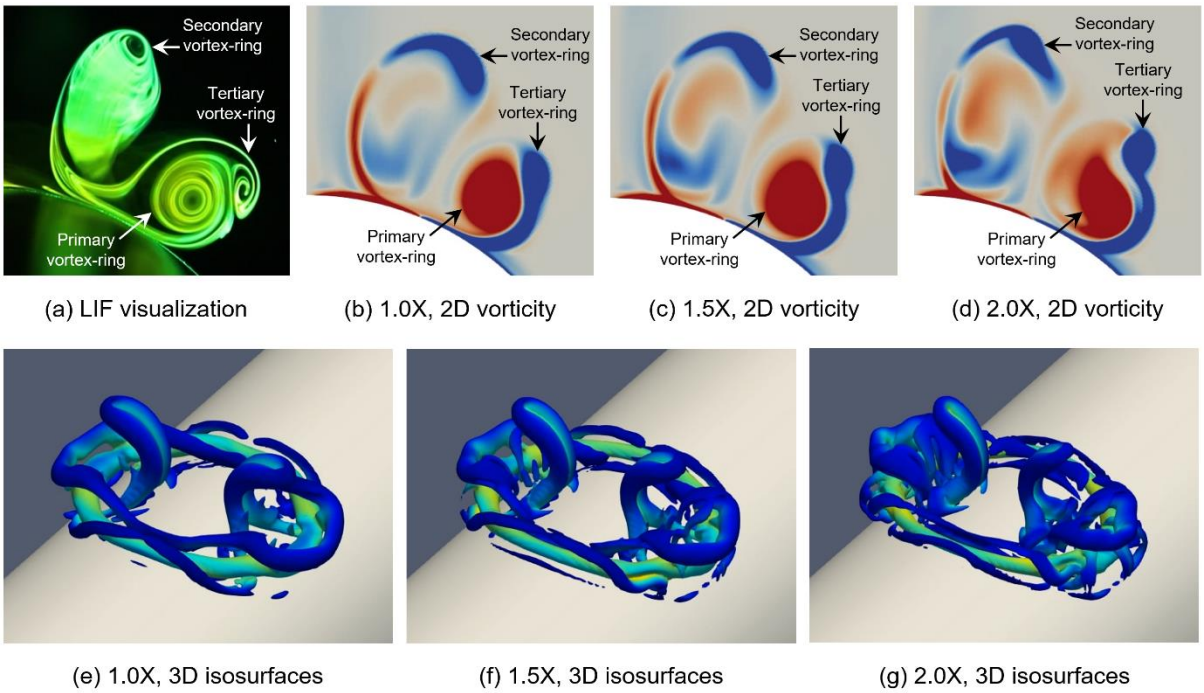

Fig. 3 (a) LIF visualization image from New and Zang (2017), 2D vorticity results from the present (b) 1.0X, (c) 1.5X and (d) 2.0X meshes, as well as their corresponding 3D isosurfaces results in (e)-(g).

As such, between the baseline and refined 1.5X meshes, the former is deemed to be sufficient as a matter of balance between modelling accuracy and computational time. Indeed, as detailed results will show later, the baseline mesh predicted transient flow results are in very good agreement with the previous experimental results.

To validate in terms of the vortex-ring structures and interactions observed during the vortex-ring collisions for the three different mesh configurations, two different comparisons will be utilized. Firstly, a 2D cross-sectional visualization image from the earlier experimental study will be compared with the 2D vorticity results along the D/d=4 cylinder convex surface at an instance where primary, secondary and tertiary vortex-rings are present and interacting. And secondly, λ_2-criterion identified 3D isosurfaces of these vortex-ring structures at the same time instance from the simulations will be compared among themselves. To start off, Fig. 3(a) shows a 2D experimental LIF visualization image that clearly shows the presence of the primary, secondary and tertiary vortex-ring cores. On the other hand, Fig. 3(b) shows the 2D vorticity results resulting from the use of the 1.0X mesh, where it

is selected to match the state depicted in Fig. 3(a) as much as possible. Subsequently, 2D vorticity plots based on 1.5X and 2.0X meshes at the same time-instance are extracted and presented in Figs. 3(c) and (d). Note that the LIF visualization image was captured at approximately τ=7, while the 2D vorticity results were extracted at τ=5. The temporal discrepancy may be attributed to the inherent differences in the initial flow conditions, where the simulations started off with an idealized vortex-ring with prescribed circulation and translation velocity. In contrast, the vortex-rings produced during the experiments were based on "cylindrical slug" approach and the discrepancy in the flow transitions is therefore not entirely unforeseen. It should also be highlighted that the emphasis of the present study is on the vortex dynamics of the collision process and the temporal discrepancy is not expected to have a detrimental impact upon the findings.

Returning to Fig. 3, the three different mesh configurations produce flow behaviour that are quite similar, despite the significant differences in the cell number used. Note that results based on the use of 1.5X and 2.0X meshes shown in Figs. 3(c) and (d) appear to produce flow behaviour that show slightly greater temporal discrepancies from the experimental result. As for the 3D isosurfaces results shown in Figs. 3(e)-(g), it can also be observed that all the key vortex structures and behaviour are relatively similar as well. In particular, partial leapfroggings of the secondary and tertiary vortex-ring segments over the primary vortex-ring can be seen, as well as the movements of the secondary vortex-ring segments towards the collision axis, as conjectured by New and Zang (2017). While increasing the mesh resolution to 1.5X and 2X over 1X do produce additional smaller-scale turbulent vortex structures, it is worth mentioning that these vortex structures do not take part significantly in the vortical interactions, nor do they contribute much to the most important flow mechanisms, as can be inferred from experimental results presented by New and Zang (2017). With a focus on the key coherent vortex structures and interactions, as well as computational costs in mind, 1.0X mesh was deemed to be satisfactory and selected to be used here for the entire study.

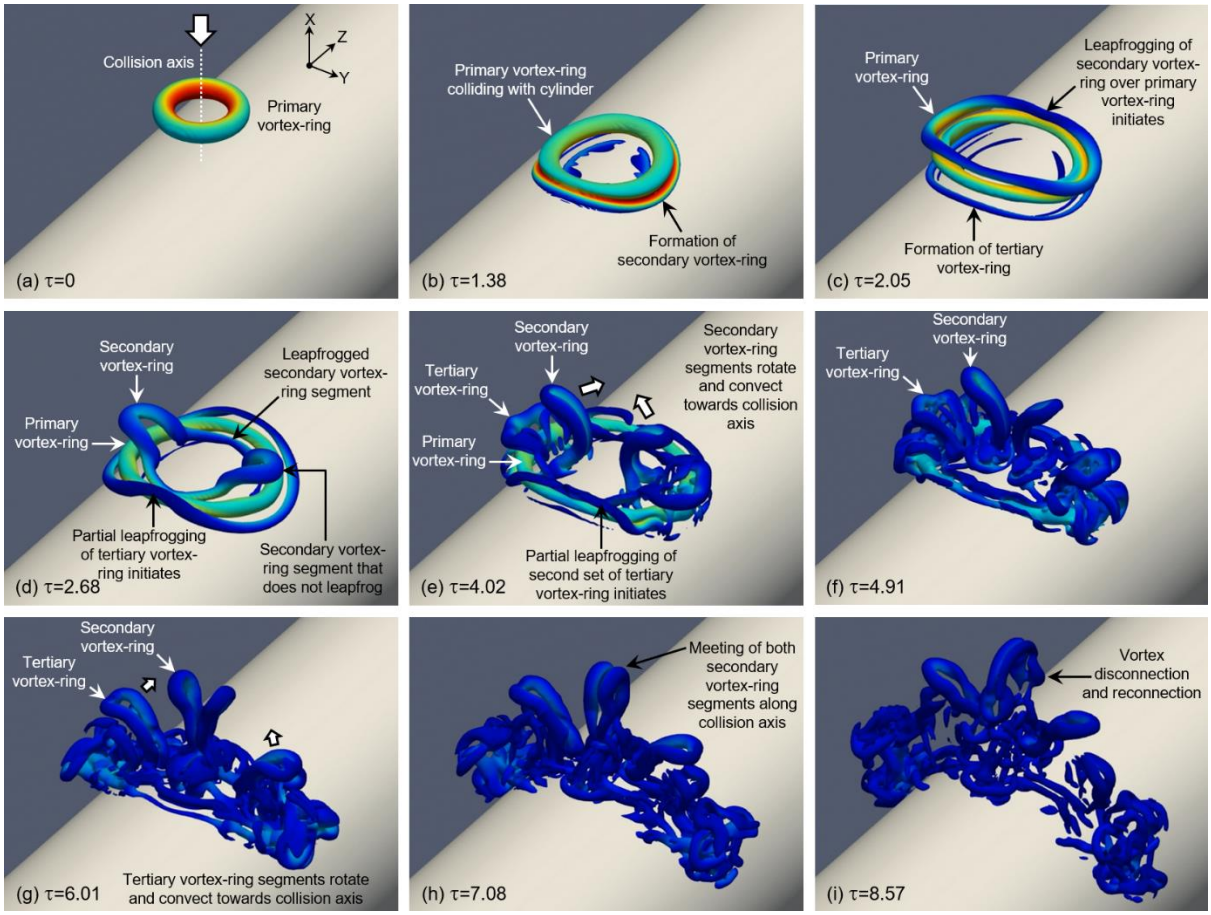

Fig. 4 Instantaneous 3D flow developments of a Re=4000 vortex-ring colliding with the D/d=4 round cylinder at (a) τ=0, (b) τ=1.38, (c) τ=2.05, (d) τ=2.68, (e) τ=4.02, (f) τ=4.91, (g) τ=6.01, (h) τ=7.08 and (i) τ=8.57.

3. Results and discussions

3.1 Vortex structures and dynamics

Figure 4 shows the instantaneous 3D flow developments associated with the collision between a Re=4000 primary vortex-ring and D/d=4 round cylinder. Note that the 3D iso-surfaces were identified and isolated based on λ_2-criterion and colour-tagged using the streamwise velocity component, u, to better differentiate the various vortex structures. Such an approach has been found to reveal the vortex dynamics of the collision process clearly, especially in the early stages here. Note that the time-intervals used are not uniform, as the goal is to highlight the most important vortical changes here. Lastly, for the sake of consistency, all results shown here start off with the primary vortex-ring located at 1d upstream of the round cylinders at τ=0.

Returning to Fig. 4, early stages of the flow developments immediately after the vortex-ring collides with the cylinder as shown in Figs. 4(a)-(c) reveal asymmetric flow behaviour and vortex structures. Due to the curvature of the cylinder, the vortex-ring comes into contact with the cylinder along the XZ-plane (i.e. straight-edge plane) before XY-plane (i.e. convex plane), which in turn leads to secondary and tertiary vortex-ring formations initiating earlier along the straight-edge plane as well. Hence, it can be readily observed that there is already a discernible phase lag in the early flow developments even for the cylinder with the smallest curvature. Thereafter, leapfrogging of secondary vortex-ring segments along the straight-edge plane and their subsequent entrainment by the primary vortex-ring segments can be discerned in Fig. 4(c). In contrast, secondary vortex-ring segments along the convex plane do not get entrained by the primary vortex-ring segment in similar fashion, but rather, appear to convect towards the collision axis without significant interactions with the primary vortex-ring segments, as shown in Fig. 4(d). It should be highlighted that at this point, tertiary vortex-ring segments are about to undergo entrainment by the primary vortex-ring segments along the straight-edge plane, and further illustrates the phase-lag between the vortical events along the straight-edge and convex planes.

As the flow proceeds, Fig. 4(e) shows the formation, leapfrogging and entrainment of a second set of tertiary vortex-ring segments by the primary vortex-ring segments along the straight-edge plane. Concurrently, secondary vortex-ring segments along the same plane also merge with the primary vortex-ring segments. In contrast, secondary vortex-ring segments along the convex plane continue to “rotate” and convect towards each other. Subsequently, as Figs. 4(f)-(i) will show, these secondary vortex-ring segments will eventually meet along the collision axis, before proceeding to pair up and move upstream along the collision axis. During this process however and intriguingly, parts of the secondary vortex-ring segments appear to undergo vortex disconnection and reconnection along the straight-edge plane, as shown in Fig. 4(i). It should also be mentioned that the first set of tertiary vortex-ring segments subsequently undergo relatively similar behaviour,

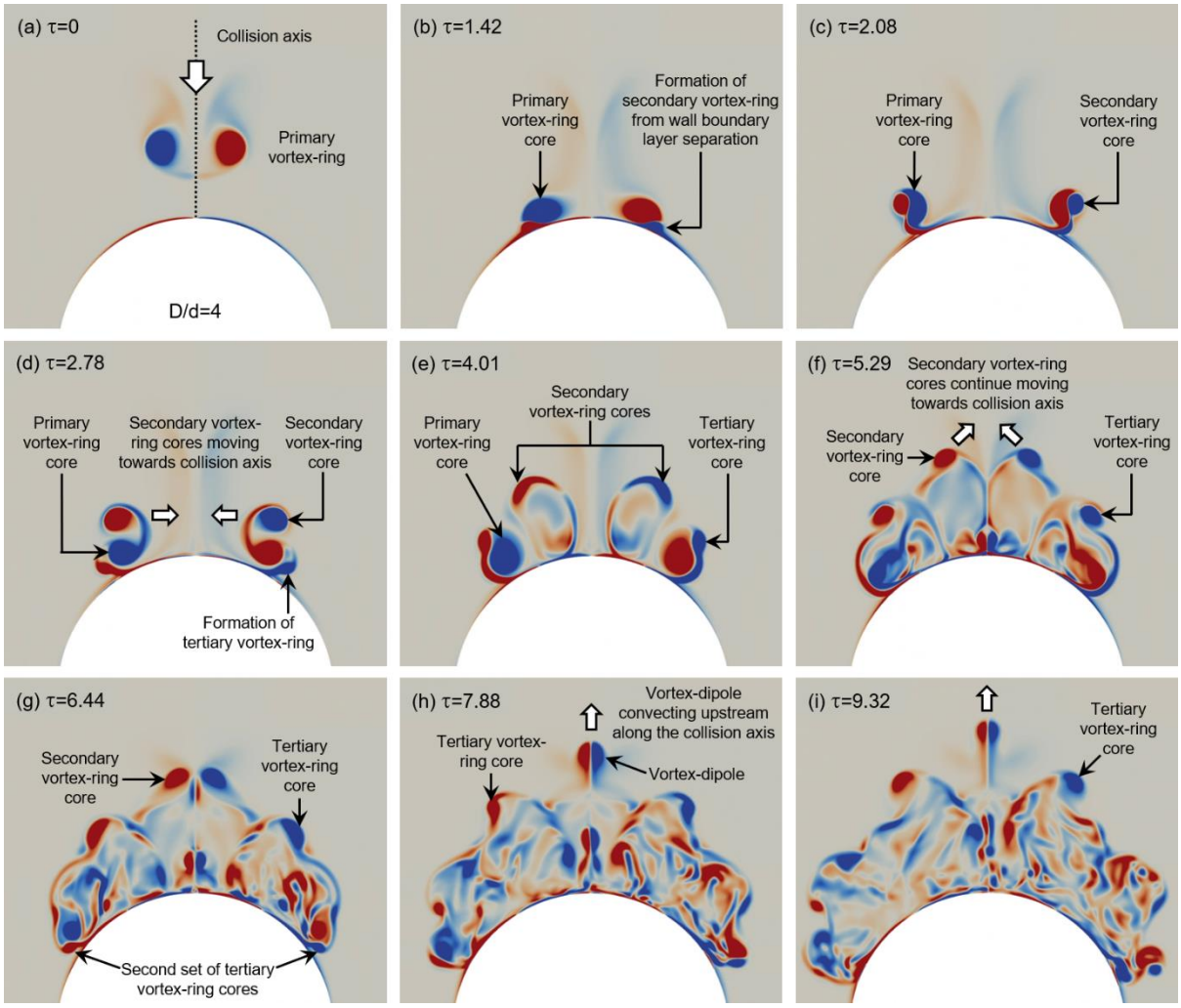

Fig. 5 Instantaneous 2D vorticity maps taken along the cylinder convex-plane of a Re=4000 vortex-ring colliding with the D/d=4 round cylinder at (a) τ=0, (b) τ=1.42, (c) τ=2.08, (d) τ=2.78, (e) τ=4.01, (f) τ=5.29, (g) τ=6.44, (h) τ=7.88 and (i) τ=9.32.

where they can be observed to rotate and convect gradually towards the collision axis.

For a closer look, Fig. 5 shows the time-sequenced 2D vorticity maps of the same flow scenario taken along the convex plane. Note that the availability of these 2D vorticity maps not only allows direct comparison with the 2D laser-induced fluorescence (LIF) results in New and Zang (2017), it will also serve as a means of validating the present numerical simulations. It can be observed from Figs. 5(a)-(c) that, when the primary vortex-ring cores collide with the convex surface, wall boundary layer separations lead to the production of secondary vortex-ring cores that leapfrog past the primary vortex-ring cores. Thereafter, the secondary vortex-ring cores move towards each other and the

collision axis, while tertiary vortex-ring cores are produced from another wall boundary layer separation along this plane, as shown in Figs. 5(d)-(e) here. As the flow continues to develop, the secondary vortex-ring cores will eventually pair up along the collisions axis to form a vortex-dipole which propagates upstream. On the other hand, the first set of tertiary vortex-ring cores can be seen to grow in size, though moving towards the collision-axis just like the preceding secondary vortex-ring cores, while a second set of tertiary vortex-ring cores begin to form from another wall boundary layer separation. Upon comparing with the experimental LIF images shown in Fig. 2 of New and Zang (2017) for the same D/d=4 cylinder, one can see good agreements in the key vortex structures and behaviour existing in the present simulation results.

Moving on to the D/d=2 cylinder shown in Fig. 6, early flow developments immediately after the vortex-ring had collided with the smaller cylinder [see Figs. 6(a)-(d)] are generally similar to those made for the larger D/d=4 cylinder. In this case however, vortical changes during the collision are proceeding at a faster rate, based on the shorter timespans with which key flow changes are observed for this cylinder, as compared to the D/d=4 cylinder. Interestingly, subsequent behaviour begins to deviate, as can be seen from Fig. 6(e) onwards. In this case, secondary vortex-ring segments along the convex plane do not rotate and move towards the collision axis after leapfrogging past the primary vortex-ring segments. Instead, they move upstream in a direction that is relatively parallel to the collision axis. Just as interesting, in Fig. 6(f) these secondary vortex-ring segments can be seen to undergo vortex disconnection and reconnection to form two distinct elliptic-like vortex-ringlets. As the flow proceeds however, filaments of these vortex-ringlets can be seen to bend in a manner that is reminiscent of axis-switching phenomenon exhibited by elliptic vortex-rings, even as they continue to travel upstream. To complement the above observations, Fig. 7 again reveals that D/d=2 and 4 cylinders lead to relatively similar flow behaviour in the early stages, especially those shown in Figs. 7(a)-(e). In particular, upstream propagation of the secondary vortex-ring segments can be observed to initiate in Fig. 7(f), before their vortex disconnection and

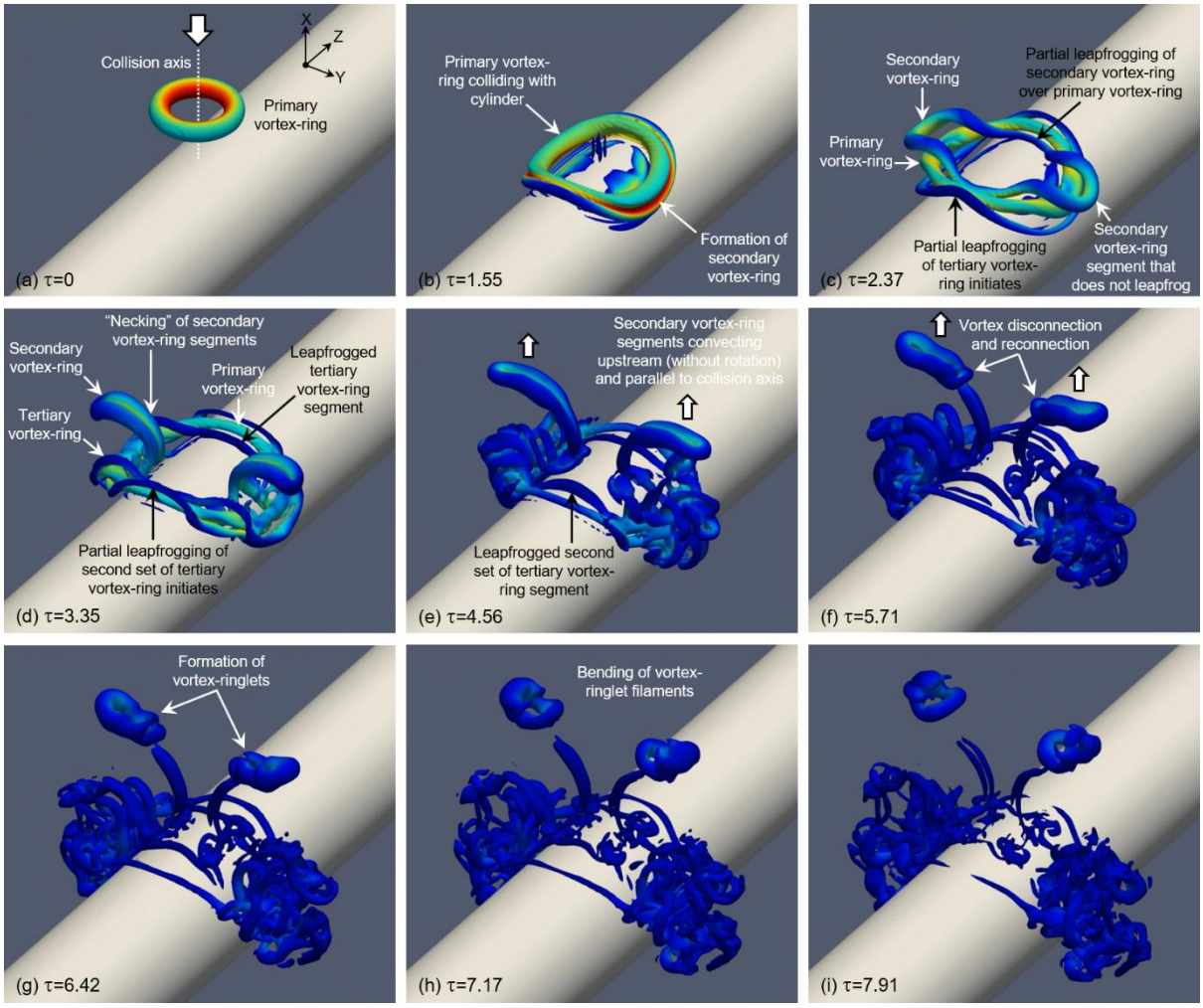

Fig. 6 3D flow developments of a Re=4000 vortex-ring colliding with the D/d=2 round cylinder at (a) τ=0, (b) τ=1.55, (c) τ=2.37, (d) τ=3.35, (e) τ=4.56, (f) τ=5.71, (g) τ=6.42, (h) τ=7.17 and (i) τ=7.91.

reconnection process produces vortex-dipoles shown in Figs. 7(h)-(i). Collating with the observations made in Fig. 6, these vortex-dipoles will be the cross-sectional manifestations of the vortex-ringlets. Experimental results presented in the previous experimental study borne these preceding numerical results out, as Figs. 7(g)-(i) are in very good agreement with Figs. 3(k), (m) and (o) of that study.

Lastly, the 3D flow dynamics associated with the smallest D/d=1 cylinder are presented in Fig. 8, where vortical changes during the collision behaviour are occurring even more rapidly now. By now, it should be clear that reducing the diameter-ratio here accelerates the flow transitions during the collisions and increasing the phase-lag in the behaviour along the convex plane and straight-edge.

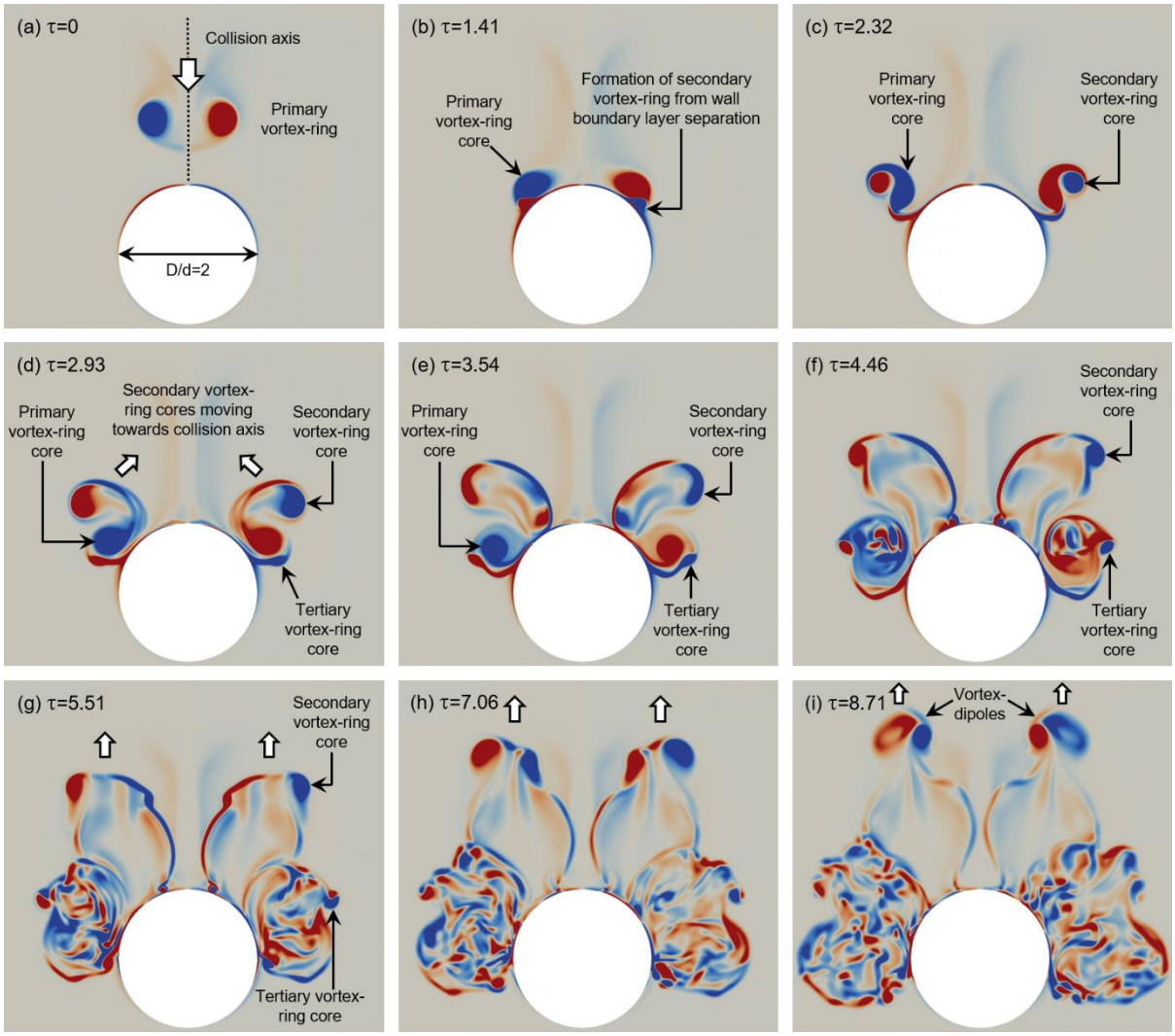

Fig. 7 Instantaneous 2D vorticity maps taken along the cylinder convex-plane of a Re=4000 vortex-ring colliding with the D/d=2 round cylinder at (a) τ=0, (b) τ=1.41, (c) τ=2.32, (d) τ=2.93, (e) τ=3.54, (f) τ=4.46, (g) τ=5.51, (h) τ=7.06 and (i) τ=8.71.

Evidences in New and Zang (2017) indicate that the phase-lag is due to the increasingly larger angle at which the wall boundary layer separates along the convex cylinder surface after the collision, which in turn points towards the cylinder diameter-ratio being a key driving factor. Nevertheless, it can be observed from Fig. 8 that the initial flow behaviour continues to be grossly similar to what had been observed for the two large cylinders, and flow deviations only happen thereafter. It is worth noting that the flow developments along the straight-edge (i.e. formation of secondary and tertiary vortex-ring, as well as their leapfrogging over the primary vortex-ring) occur significantly earlier than those along the convex plane for this smallest cylinder. In fact, the much slower flow

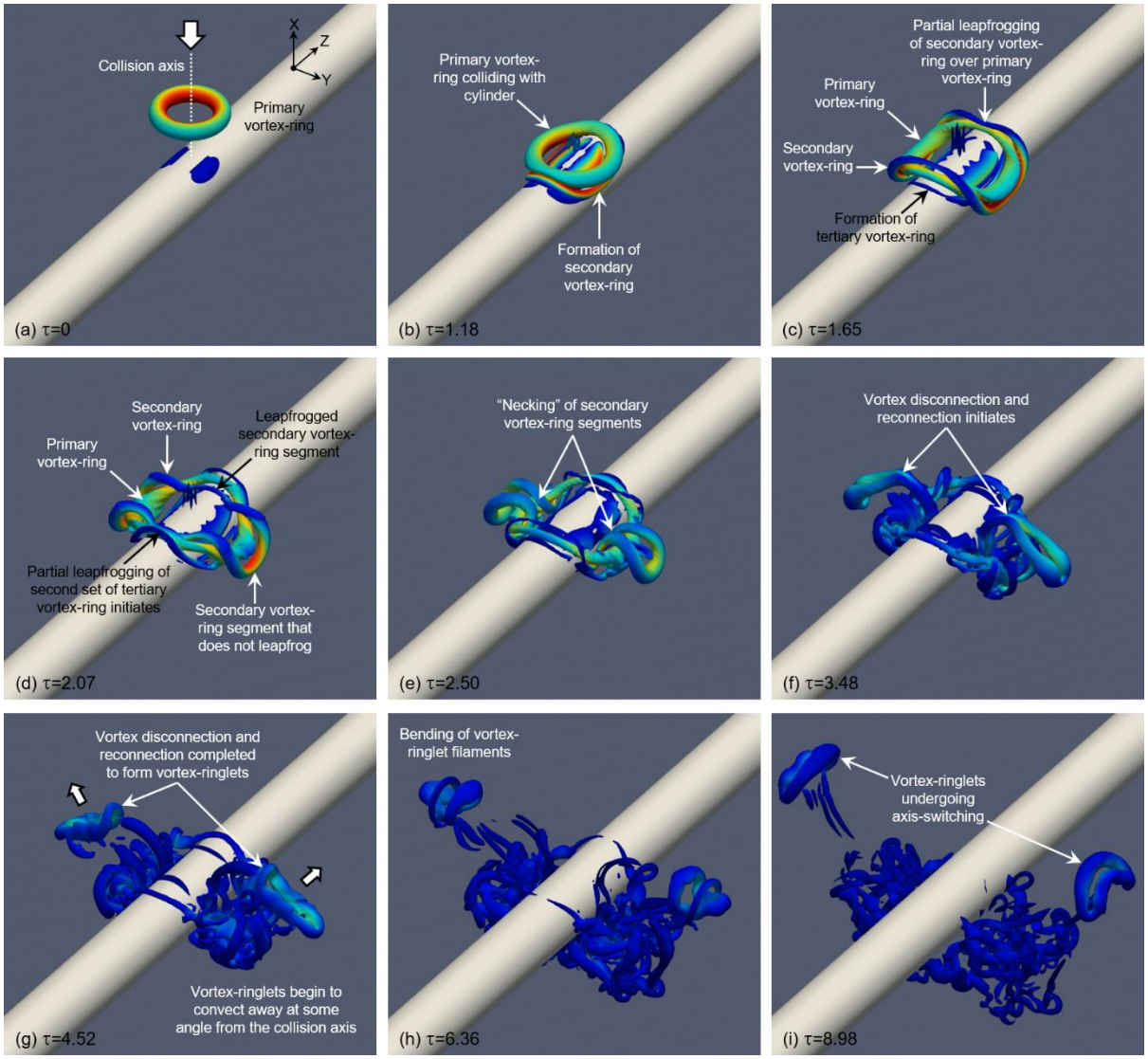

Fig. 8 3D flow developments of a Re=4000 vortex-ring colliding with the D/d=1 round cylinder at (a) τ=0, (b) τ=1.18, (c) τ=1.65, (d) τ=2.07, (e) τ=2.50, (f) τ=3.48, (g) τ=4.52, (h) τ=6.36 and (i) τ=8.98.

progressions along the convex plane meant that the secondary vortex-ring segments do not leapfrog past the primary vortex-ring segments there at all. Note that while this is distinctively different from D/d=2 and 4 cylinders earlier on, Figs. 8(e)-(i) show that the basic flow behaviour remains fundamentally comparable to those seen for D/d=2 cylinder with a few notable exceptions.

Case in point, Figs. 8(e)-(f) show that the non-leapfrogging secondary vortex-ring segments along the convex plane remain physically beyond the confines of the primary vortex-ring segments, while flow

events are taking place rapidly along the straight-edge. In particular, Fig. 8(e) suggests that severe "necking" of the secondary vortex-ring segments near the primary vortex-ring segments occurs, presumably due to interactions between these vortex-ring segments and induced flows set up by the rapid leapfrogging and entrainment processes along the straight-edge. After that, the secondary vortex-ring segments undergo vortex disconnection/reconnection to produce two elliptic-like vortex-ringlets that move away from the cylinder. It should also be clear from Fig. 8(g)-(i) that the vortex-ringlets travel away from the cylinder at a certain angle symmetrically about the collision axis, with their filaments undergoing bending at the same time. Lastly, vorticity maps presented in Fig. 9 show how the vortex-ringlets manifest as vortex-dipoles after they are formed, which then travel away from and upstream of the cylinder at some angle. Comparing with Fig. 4 of New and Zang (2017), the present simulation reproduces flow behaviour that was captured experimentally in the earlier study. To better illustrate this point, instantaneous vorticity maps are now presented in Fig. 9.

Figure 9 confirms that the very early stages of the flow development immediately after the primary vortex-ring collides remain grossly similar with D/d=2 and 4 round cylinders. Specifically, the formations of the secondary and tertiary vortex-ring cores occur shortly thereafter. In this case however, the secondary and tertiary vortex-ring cores are not close to being entrained by the primary vortex-ring cores along this plane at all. Part of the reason is because they are initiated much later along the D/d=1 round cylinder convex surface. These are in good agreement with Fig. 4(g) of New and Zang (2017), including the experimentally-observed "rebounding" behaviour that appears in Fig. 9(f). Most importantly, the present simulations accurately predicted not only the two pairs of vortex-dipoles that are observed to form at the later stages of the flow scenario during the experiments but also that they travel upstream and away from the smallest round cylinder at significant angles away from the collision axis (see Fig. 4(k)-(o) of New and Zang (2017)), as shown in Figs. 9(j) and (k). Having said that, there is a discrepancy between the predicted trajectory of the vortex-dipoles and that observed experimentally. The trajectory was estimated to be approximately

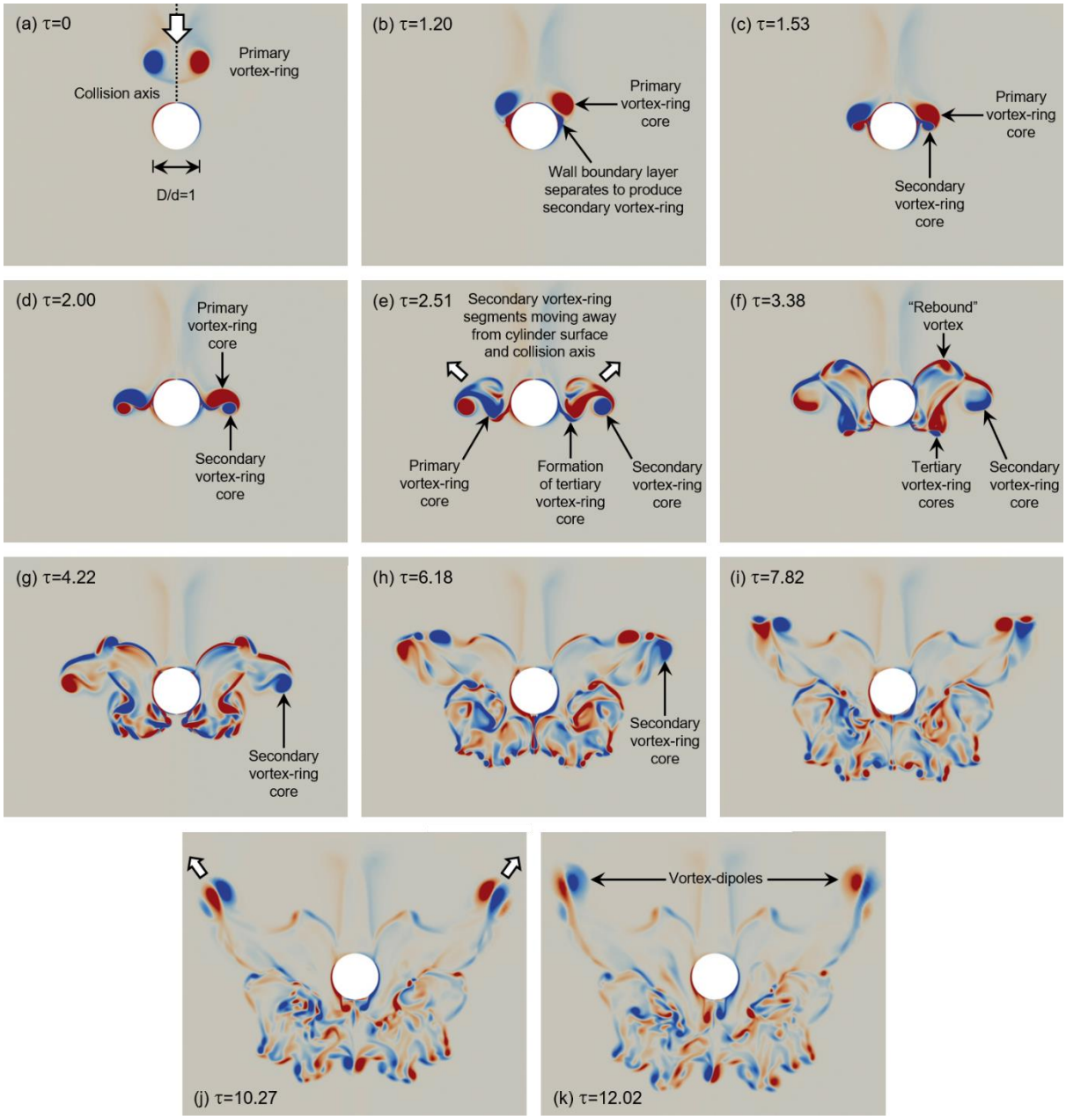

Fig. 9 Instantaneous 2D vorticity maps taken along the cylinder convex-plane of a Re=4000 vortex-ring colliding with the D/d=1 round cylinder at (a) τ=0, (b) τ=1.20, (c) τ=1.53, (d) τ=2.00, (e) τ=2.51, (f) τ=3.38, (g) τ=4.22, (h) τ=6.18, (i) τ=7.82, (j) τ=10.27 and (k) τ=12.02.

60° away from the collision axis based on 2D flow visualization and measurement results by New and Zang (2017) but the present simulations predict a lower angular value of approximately 55° as will be shown later.

At this point, it will be timely to take a closer look at the 2D vorticity distributions along the cylinder straight-edges (i.e. z-direction). As shown in Figs. 10-12 of New and Zang (2017), experimental results revealed that the cross-sections of the vortex-ring collision processes for all round cylinders taken along the cylinder straight-edge are mostly insensitive towards the exact diameter-ratio used. In particular, their 2D laser-induced fluorescence showed that the cross-sections along the straight-edge closely resemble that produced by a vortex-ring colliding head-on with a flat-surface (New et al., 2016), rather than the more complex dynamics observed along the convex surface. In addition, a common but interesting behaviour observed in that study would be the rapid reductions in the primary and secondary vortex-ring core sizes, indicative of elevated vortex-stretching of the main vortex structures around the convex surfaces. Hence, it will be more intuitive to group all the results taken along the straight-edge together for discussions here and see if the present simulations are able to yield additional flow details.

Figure 10 shows the 2D vorticity maps taken along the straight-edge of D/d=4 round cylinder at the same timings as those shown in Fig. 5. As mentioned before and as the figure shows, the initial flow stages after the primary vortex-ring collides with the cylinder are quite similar to those for flat surface-based vortex-ring collisions, as can be seen in Figs. 10(a)-(e). At this point, the secondary and tertiary vortex-ring cores have been entrained by the primary vortex-ring cores. As the flow develops, the secondary and tertiary vortex-ring cores subsequently merge as one from Fig. 10(g) onwards. It should also be clear from inspecting the time-sequenced results that all the vortex-core sizes become increasingly smaller during the collision process, more so than the situation observed for vortex-rings colliding upon flat surfaces under the exact same flow configurations (New et al., 2016). This behaviour is, in fact, in good agreement with and validated by similar observations by New and Zang (2017). However, due to the availability of only 2D results, the preceding study could only postulate that such a behaviour may be attributed to vortex-stretching of the primary, secondary and tertiary vortex-ring segments around the convex surface. Now, with the 3D vortex

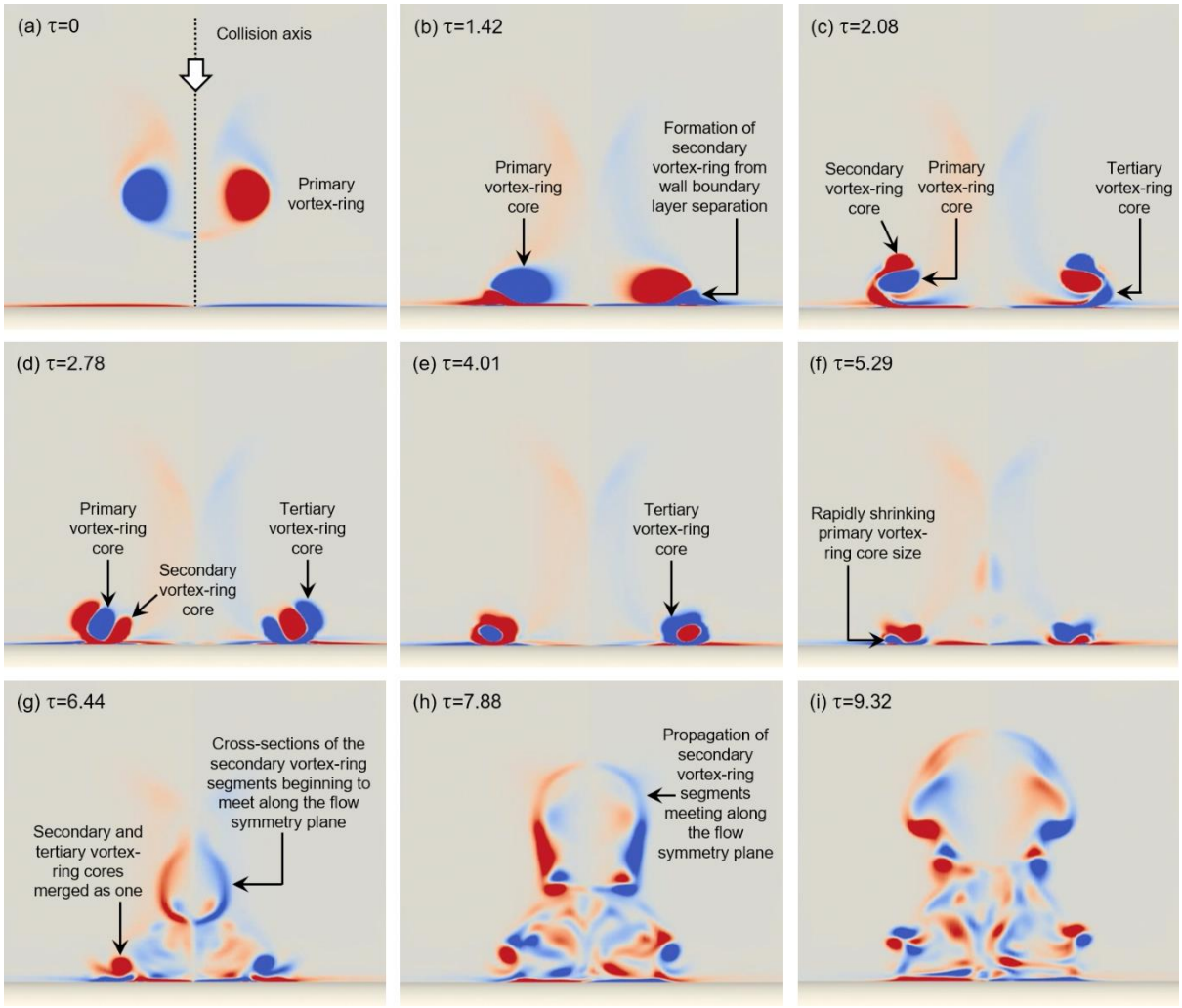

Fig. 10 Instantaneous 2D vorticity maps taken along the cylinder straight edge-plane of a Re=4000 vortex-ring colliding with the D/d=4 round cylinder at (a) τ=0, (b) τ=1.42, (c) τ=2.08, (d) τ=2.78, (e) τ=4.01, (f) τ=5.29, (g) τ=6.44, (h) τ=7.88 and (i) τ=9.32.

structures presented in Fig. 4, it can be observed that the primary, secondary and tertiary vortex-ring segments do indeed undergo vortex-stretching around the convex surface of the D/d=4 round cylinder after the primary vortex-ring collided with it. As such, the general curvature of the overall vortex structures can be seen to increase as the flow develops, especially in Figs. 10(h)-(i).

It should be highlighted that the present simulation results reveal behaviour that was not captured by New and Zang (2017). Particularly, Figs. 10(g)-(i) shows the emergence of additional vortical activities above the straight-edge that do not show up in the experimental results. Upon closer inspection and correlating with the 3D isosurface results in Fig. 4, it can be deduced that these

vortex structures are actually cross-sections of the secondary vortex-ring segments that are approaching each other along the straight-edge plane. Indeed, as they move towards and meet each other gradually as depicted in Figs. 4(g)-(i), the vorticity regions above the straight-edge becomes increasingly more prominent and depicts the entire process that leads to the production of a 2D vortex-dipole that eventually travel upstream along the collision axis (see Figs. 5(g)-(i)). This is of importance as the vortex model put forward in New and Zang (2017) utilized similar concepts in an attempt to explain their 2D flow results. As a result, the present simulation results largely support the notions raised in the earlier study thus far.

Having said that, there is one notable discrepancy between the present simulations and the earlier experimental results as well. In particular, the formation of a vortex-ringlet at the later stages of the flow after the secondary vortex-ring segments meet along the straight-edge plane as postulated by the vortex model (see Fig. 19(f) of New and Zang, 2017) does not show up in the present simulation. However, that could very well be due to the inherent differences in the present idealized vortex-rings, as opposed to those produced via a piston-driven "cylindrical slug" approach adopted by the earlier experimental study, where they would lead to differences in the initial vortex-ring circulation and its uniformity. Nevertheless, this should be investigated further in future studies since it could materially impact upon the resulting heat transfer characteristics should the present scenario be extended to one that considered heat transfer to/from a large diameter-ratio round cylinder. One possibility will be to model the actual vortex-ring generation within the nozzle and further upstream with the experimental piston velocity profiles implemented, similar to what had been adopted by Le et al. (2011) for their impulsively produced vortex-rings.

Moving on to the D/d=2 and 1 round cylinders, Figs. 11 and 12 depict flow behaviour very similar to those observed experimentally by New and Zang (2017) with little discrepancies. In this case, other than resembling flat surface-based vortex-ring collisions, there are no vorticity regions that indicate

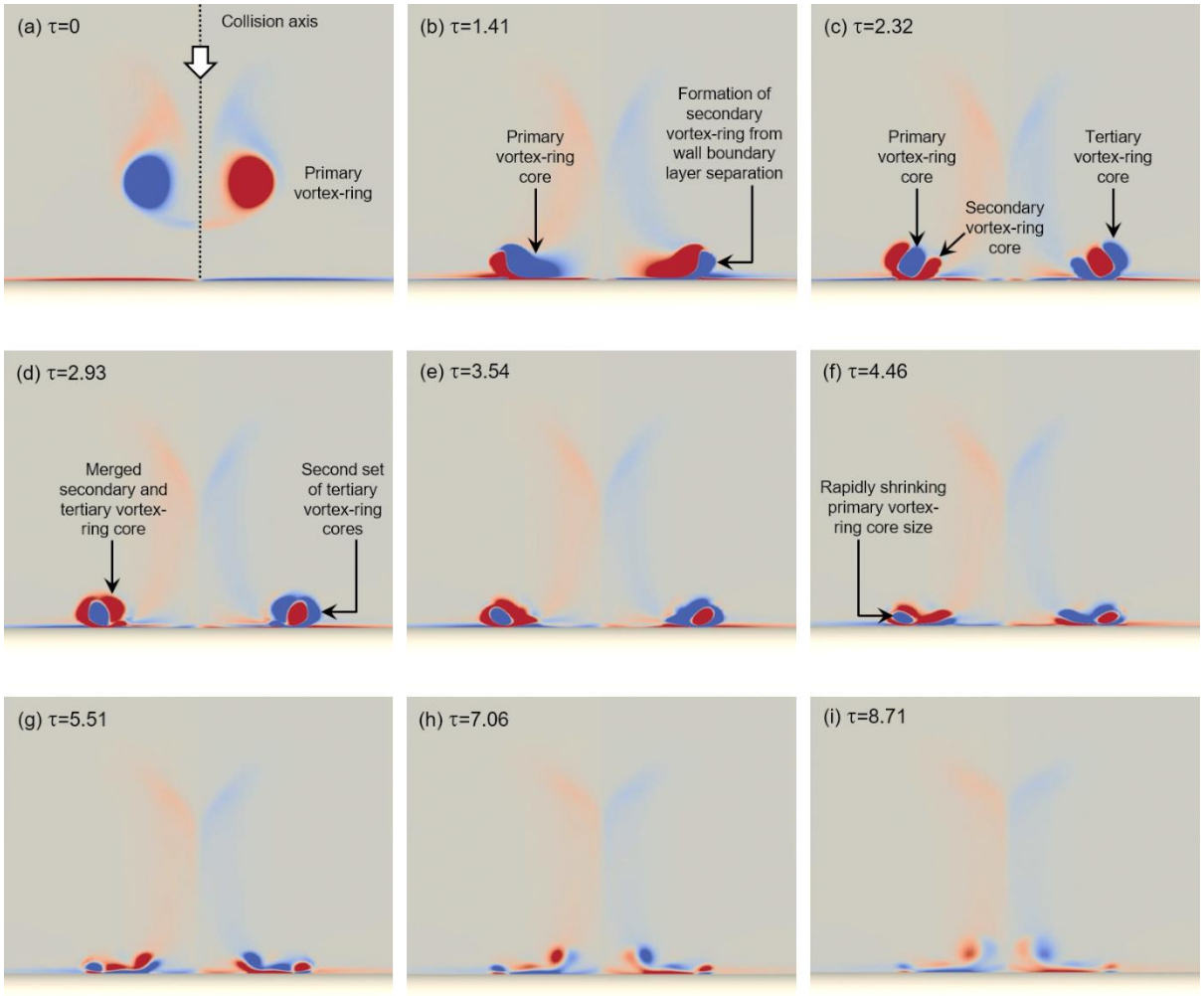

Fig. 11 Instantaneous 2D vorticity maps taken along the cylinder straight edge-plane of a Re=4000 vortex-ring colliding with the D/d=2 round cylinder at (a) τ=0, (b) τ=1.41, (c) τ=2.32, (d) τ=2.93, (e) τ=3.54, (f) τ=4.46, (g) τ=5.51, (h) τ=7.06 and (i) τ=8.71.

movements of secondary (or tertiary) vortex-ring segments towards the straight-edge plane for both configurations. Furthermore, results also show that the reduction in the various vortex-core sizes picks up speed as the diameter-ratio decreases from D/d=2 to 1, as evident from the progressively shorter times taken for the core size reductions. As such, the experimentally observed vortex structures and their mutual interactions are well-predicted for these two round cylinders by the present simulations. The lack of vorticity regions above the straight-edge such as those observed for the D/d=4 round cylinder is due to the fact that the secondary vortex-ring segments move towards the upstream direction for the D/d=2 round cylinder, as well as away from the collision axis for the

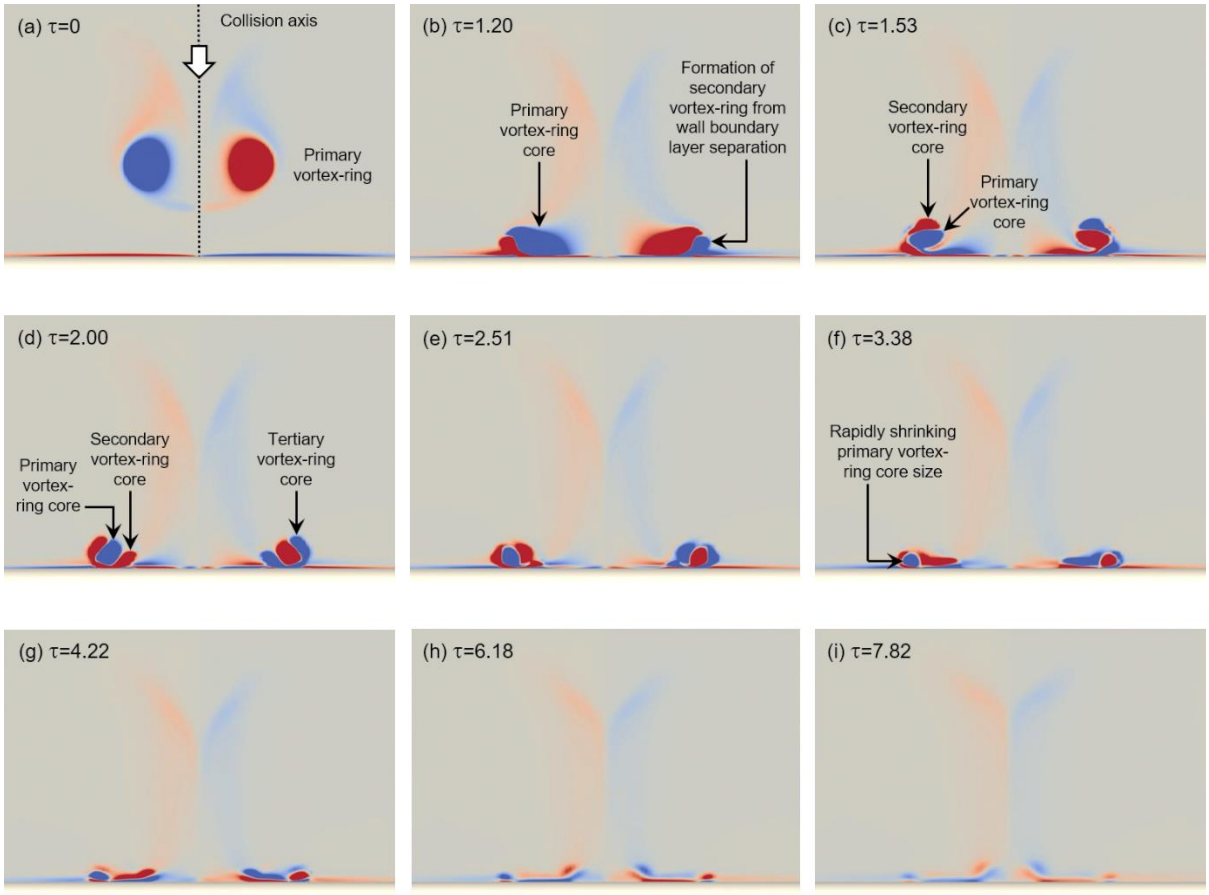

Fig. 12 Instantaneous 2D vorticity maps taken along the cylinder straight edge-plane of a Re=4000 vortex-ring colliding with the D/d=1 round cylinder at (a) τ=0, (b) τ=1.20, (c) τ=1.53, (d) τ=2.00, (e) τ=2.51, (f) τ=3.38, (g) τ=4.22, (h) τ=6.18 and (i) τ=7.82.

D/d=1 round cylinder. There could be no manifestations of their cross-sections along the straight-edge plane in that case.

3.2 Vortex-core trajectories

Preceding comparisons have shown good agreement between the present simulation results and earlier experimental findings. However, one of the most important and commonly sought-after information with respect to discrete vortex-ring collisions will be the vortex-core trajectories. Since vortex-rings may be considered as the fundamental flow components of freely-exhausting hot/cold jets, better comparison and hence modelling of the vortex-core trajectories will contribute towards improving heat and mass transfer applications such as jet-based heating and cooling of round-

shaped manufactured products. As such, trajectories of key vortex-cores associated with primary, secondary and tertiary vortex-rings, as well as others produced during the collisions, are extracted from the 2D instantaneous vorticity results along both the convex surface and straight-edge for all round cylinders here and compared with the earlier experimental results. Note that along the straight-edge planes, other than the primary vortex-ring core trajectories which were sampled at intervals of τ=0.12, the other vortex-core trajectories were sampled at intervals of τ=0.24 or 0.36 to avoid data clutter in the plots. On the other hand, trajectories taken along the convex cylindrical surfaces were all sampled at intervals of τ=0.12 throughout, due to the significant larger vortical movements along this plane.

It should be highlighted that the availability of simulation results here could provide certain benefits over experimental results in terms of extracting vortex-core trajectories. Firstly, there exist certain limitations in the use of scalar dyes to track vortex structures and their core locations, the latter of which should ideally be tracked based on velocity fields or flow quantities based on velocity fields. Secondly, New and Zang (2017) had earlier revealed the rapid reductions in vortex-core physical sizes taking place along the straight-edge planes, and simulation results could potentially better track the vortex-cores when they become increasingly smaller, as compared to flow visualizations and PIV measurements. Thirdly, the time-step used during the present simulations are significantly smaller than the sampling rates used by New and Zang (2017) in their flow visualizations and PIV measurements, which means that higher fidelity temporal results (and hence, vortex-core tracking) could be obtained here. Last but not least, simulation results here allow significantly larger flow areas for vortex-core tracking, as compared to the more constrained flow areas typically faced by experimental approaches, computational time notwithstanding.

It should be mentioned here that trajectory results taken along the straight-edge plane will be discussed first due to their gross similarities regardless of the exact diameter-ratio. Figure 13 shows

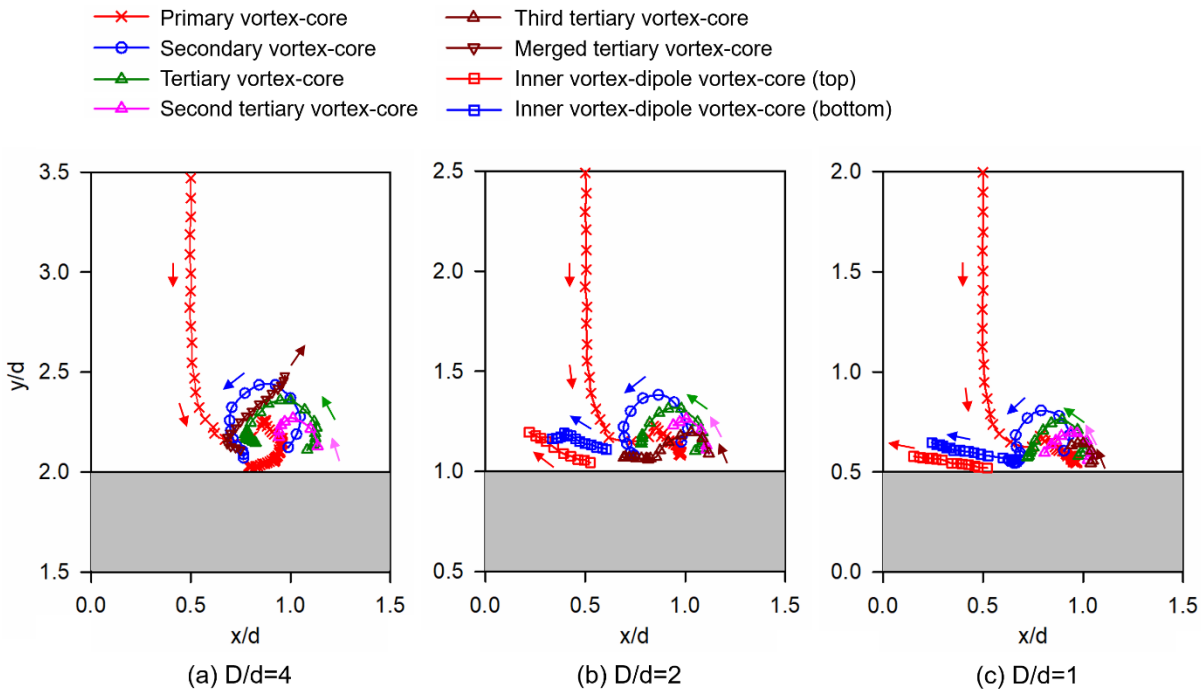

Fig. 13 Trajectories of key vortex-cores observed along the straight-edge planes of (a) D/d=4, (b) D/d=2 and (c) D/d=1 round cylinders.

these results and indeed, not only are their general trajectories quite similar between them, most of their aspects also closely resemble to those observed for round vortex-rings colliding normally with flat-surfaces previously, such as those observed by Lim (1989), Orlandi and Verzicco (1993), Cheng et al. (2010) and New et al. (2016). For instance, the primary vortex-ring cores will move away from the collision axis after the collision, while the secondary and tertiary vortex-ring cores will be entrained into the confines of the primary vortex-ring cores. This is particularly the case for the largest diameter-ratio cylinder where its geometry is closest to a flat-surface, which should not come as a surprise. These similarities surround the trajectories of the primary, secondary and tertiary vortex-ring cores, though specific key differences can be observed as well. For the D/d=4 cylinder as shown in Fig. 13(a), it produces a second set of tertiary vortex-ring cores which merged with the first set of tertiary vortex-ring cores (to produce the merged tertiary vortex-core) while they are within the confines of the primary vortex-ring cores. The merged vortex-core will then subsequently travel upwards and away from the straight-edge.

As for the D/d=2 and 1 cylinders, their behaviour are very similar to each other but differ from that of the D/d=4 cylinder. Firstly, Figs. 13(b) and (c) show that the two smaller diameter-ratio cylinders actually produce three sets of tertiary vortex-ring cores that are subsequently entrained by the primary vortex-ring cores. Secondly, in each of these cylinders, these tertiary vortex-ring cores merge within the confines of the primary vortex-ring core but the merged tertiary vortex-core does not travel away from the straight-edges (much like what has been observed for the D/d=4 cylinder earlier). Instead and interestingly, the merged tertiary vortex-core travels along the straight-edge towards the collision axis. This in turn causes the inner wall boundary layer to separate to produce a wall-separated vortex, which together with the merged tertiary vortex-core, form a vortex-dipole that appears to move gradually along the inner wall region. These observations reinforce the notion put forward by New and Zang (2017) that the present vortex-ring collision mechanisms are different between D/d=4 cylinder and D/d=2, 1 cylinders, which give further confidence to the validity of the present simulations.

Next, Fig. 14 shows the corresponding trajectory results taken along the cylinder convex surfaces. Comparing with the experimental results obtained by New and Zang (2017), good agreements in the trajectories of the primary, secondary, tertiary and rebound (or dipole) vortex-cores can be observed. Additionally, trajectories of the second set of tertiary vortex-ring cores can be successfully identified and tracked through the simulation results, even though they do not engage significantly in the key vortex dynamics here. It should also be highlighted that trajectories of the vortex-dipoles produced by the D/d=2 and 1 cylinders along this plane agree with those observed by the earlier experimental studies, despite the differences in the initial flow conditions adopted by the present simulations and previous experiments. In particular, the trajectory of the vortex-dipole for D/d=1 cylinder is estimated to be approximately 55°, as compared to the approximately 60° estimated by New and Zang (2017). Again, considering the vortex-ring initialization differences between the simulations and the earlier experiments, the agreement is deemed to be reasonable.

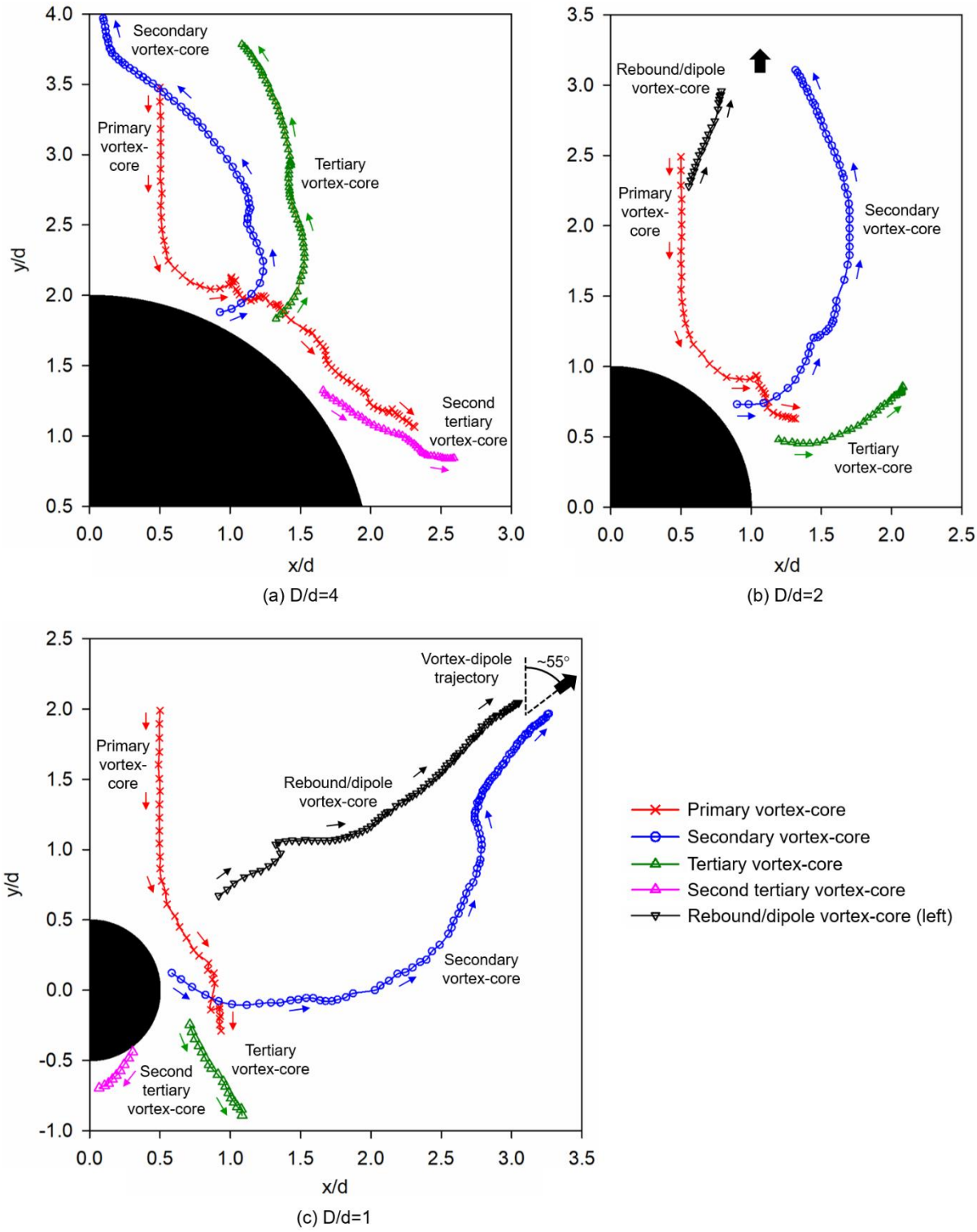

Fig. 14 Trajectories of key vortex-cores observed along the convex surfaces of (a) D/d=4, (b) D/d=2 and (c) D/d=1 round cylinders.

New and Zang (2017) attributed the differences in the vortex-dipole trajectories as the diameter-ratio varies to the differences in the locations along the cylinder convex surface at which secondary vortex-ring cores are first formed. With the availability of the present simulation results, it will be

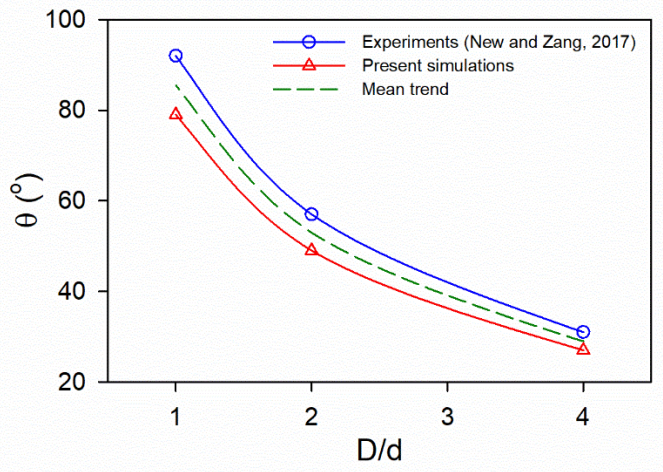

Fig. 15 Comparison of secondary vortex-ring core formation locations along the cylinder convex surfaces for all diameter-ratios between present simulations and past experiments (New and Zang 2017).

timely to compare to what extent do the secondary vortex-ring core formation locations along the convex surfaces between the simulation and experimental results agree. In that case, using the collision axis as a reference (i.e. θ=0°), the secondary vortex-ring core formation locations, θ, are subsequently plotted against the diameter-ratio and presented in Fig. 15. As can be seen from the figure, there exist satisfactory agreement between the past experimental and present simulation results in terms of the trends, with the latter predicting smaller angular locations at which secondary vortex-ring cores are formed. In particular, note that the differences in the angular locations for D/d=4, 2 and 1 cylinders are 4°, 8° and 13° respectively. These preceding observations can be attributed to, firstly, the inherent flow differences between a piston-driven experimentally produced vortex-ring and one that is initialized ideally during the simulation. Secondly, the increasingly larger angular discrepancy when the diameter-ratio reduces points towards a continuing gap in the accurate modelling of complex vortex dynamics here, especially when more convoluted and higher levels of vortex-stretching exist as the diameter-ratio decreases.

The preceding findings have several important implications for heat transfer applications that make use of continuous or intermittent jets for heating or cooling cylindrical-shaped objects. As mentioned earlier, these vortex-rings can be treated analogously to the ring-vortices formed readily by jet flows. Firstly, the diameter of the cylindrical-shaped object relative to that of the jet (i.e.

diameter-ratio) has a strong influence over the effective surface area coverage. From Fig. 14, it can be inferred that the larger the relative diameter of the cylindrical object, the lower the proportion of its cylindrical surface area that will be heated or cooled by the jets. This is due to the small angular displacement and hence relatively short distance travelled along the convex surface by the primary vortex-ring before its cores move away from the convex surface when the diameter-ratio is D/d=2 and above. These present vortex-ring based observations are further reinforced by the observations made by New and Long (2015), as well as Long and New (2015, 2019), when they investigated jet impingements upon similarly sized round cylinders. As such, they suggest lower levels of heating/cooling and reduced heat transfer efficiency than what the jet flows are potentially able to provide when the cylindrical object diameters are significantly larger than the jet diameters.

Secondly, relatively larger cylindrical objects could lead to reverse flows that interfere with the proper functioning of intermittent heating/cooling jet flows. As can be seen in Fig. 14, secondary and tertiary vortex-ring cores of the D/d=4 cylinder and the vortex-dipole cores of the D/d=2 cylinders travelled upstream after the collisions. Such upstream movements indicate that intermittent heating/cooling jet flows could very well face significant flow blockages and/or stability issues that affect their efficacy when comparatively larger cylindrical-shaped objects are used, particularly at high Reynolds numbers. In contrast, there is better flow coverage over the D/d=1 cylinder convex surface by the vortex-ring and the movements of the vortex-dipole cores are at a significant angle away from the collision axis. Based on the above considerations, New and Zang (2017) and the present study suggest that the jet and cylindrical-shaped object diameters should be comparable for optimal heating/cooling outcomes. Nonetheless, further studies based on heat transfer related measurements should be conducted to validate the preceding flow observation based postulations.

4. Conclusions

A numerical simulation study was conducted to reveal more details upon the vortex dynamics associated with a circular vortex-ring colliding perpendicularly upon the convex surfaces of three round cylinders with diameter-ratios of D/d=4,2 and 1 at Re=4000. Considering the differences in the vortex-ring formation mechanism between the past experiment by New and Zang (2017) and present simulation, good agreements between them are observed. The present simulations confirm that increasingly higher levels of vortex-stretching occur as the diameter-ratio reduces, which impact directly upon the subsequent formations of the secondary and tertiary vortex-rings. Reductions in the diameter-ratio also lead to increasing phase-lags between the vortical behaviour along the cylinder convex surface and straight-edge planes, as well as large angular locations at which the secondary vortex-ring cores are formed along the convex surfaces. These result in very different flow outcomes from the interactions between the primary, secondary and tertiary vortex-rings, where the use of the largest diameter-ratio cylinder here (i.e. D/d=4) sees two opposing secondary vortex-ring segments moving towards to meet each other to produce a small vortex-dipole. On the other hand, the use of D/d=2 and 1 cylinders will not see the two secondary vortex-ring segments moving towards each other. Instead, the secondary vortex-ring segments undergo vortex disconnection/reconnection processes that resemble a “pinching-off” process that see them transforming into two elliptic vortex-ringlets for each of the smaller cylinders. These vortex-ringlets move towards the upstream direction and approximately parallel to the collision axis for the D/d=2 cylinder, but upstream and approximately 55° from the collision axis for the D/d=1 cylinder. Interestingly, the aspect ratio of the vortex-ringlets increases when the diameter-ratio decreases from 2 to 1, most likely a result of heightened vortex-stretching levels due to the very high curvature of the smallest D/d=1 cylinder. In fact, the vortex-ringlets appear to undergo axis-switching as the flow develops for this particular cylinder.

The present simulations allow good tracking of the key vortex-ring core trajectories along the cylinder convex surfaces and straight-edges despite the complex vortex dynamics and vortex-stretching behaviour, particularly the case for smaller tertiary vortex-ring cores which experimental approaches may find challenging. Results along the convex surfaces show good agreements with the past experimental study, especially with the predicted vortex-dipole trajectory for the D/d=1 cylinder at approximately 55° away from the collision axis as compared to about 60° based the past experimental study. Finally, secondary vortex-ring core formation locations, which are postulated to account for the flow differences for the different cylinders, are also observed to be comparable between the present simulations and past experimental study. Despite demonstrating very similar trends with the past experimental results, it should be noted that the simulations consistently under predict the angular values of these formation locations and may again be attributed to the differences in the vortex-ring initializations between present simulations and past experiments. Last but not least, present and earlier flow observations suggest that cylinder and impinging jet diameters should be comparable for more optimal practical heat transfer outcomes. Cylinders with comparatively larger diameters than the jet flows are likely to have relatively lower surface coverage due to earlier flow separations along the cylindrical surfaces, as well as potentially destabilizing flow effects for intermittent jet flows.

Acknowledgement

The authors acknowledge the support provided by the School of Mechanical and Aerospace Engineering, Nanyang Technological University, for the study, computational resources provided by the National Supercomputing Centre, Singapore (NSCC) for the simulations, and support from Technical University of Munich for the second author.

Data availability statement

The data that support the findings of this study are available from the corresponding author upon reasonable request.

References

Adhikari, D., & Lim, T. T. (2009). The impact of a vortex ring on a porous screen. Fluid Dynamics Research, 41(5), 051404.

Ahmed, T., & Erath, B. (2020). Experimental investigation of a vortex ring impinging on a concave cavity. Bulletin of the American Physical Society, 65.

Cheng, M., Lou, J., & Luo, L. S. (2010). Numerical study of a vortex ring impacting a flat wall. Journal of Fluid Mechanics, 660, 430.

Cheng, M., Lou, J., & Lim, T. T. (2014). A numerical study of a vortex ring impacting a permeable wall. Physics of Fluids, 26(10), 103602.

Chu, C. C., Wang, C. T., & Chang, C. C. (1995). A vortex ring impinging on a solid plane surface—Vortex structure and surface force. Physics of Fluids, 7(6), 1391-1401.

Couch, L. D., & Krueger, P. S. (2011). Experimental investigation of vortex rings impinging on inclined surfaces. Experiments in fluids, 51(4), 1123-1138.

Fabris, D., Liepmann, D., & Marcus, D. (1996). Quantitative experimental and numerical investigation of a vortex ring impinging on a wall. Physics of Fluids, 8(10), 2640-2649.

Hu, J., & Peterson, S. D. (2018). Vortex ring impingement on a wall with a coaxial aperture. Physical Review Fluids, 3(8), 084701.

Hu, J., & Peterson, S. D. (2021). Hydrodynamic impulse enhancement of a vortex ring interacting with an axisymmetric co-axial aperture. Journal of Fluid Mechanics, 917.

Hrynuk, J. T., Stutz, C. M., & Bohl, D. G. (2018). Experimental measurement of vortex ring screen interaction using flow visualization and molecular tagging velocimetry. Journal of Fluids Engineering, 140(11).

Hrynuk, J. T., Van Luipen, J., & Bohl, D. (2012). Flow visualization of a vortex ring interaction with porous surfaces. Physics of Fluids, 24(3), 037103.

Issa, R. I. (1986). Solution of the implicitly discretised fluid flow equations by operator-splitting. Journal of Computational Physics, 62(1), 40-65.

Jiang, X., & Lai, C. H. (2016). Numerical techniques for direct and large-eddy simulations. CRC Press.

Lamb, H. (1993). Hydrodynamics. Cambridge University Press.

Le, T. B., Borazjani, I., Kang, S., & Sotiropoulos, F. (2011). On the structure of vortex rings from inclined nozzles. Journal of Fluid Mechanics, 686, 451.

Li, Q., & Bruecker, C. H. (2018). Vortex interaction with a rough wall formed by a hexagonal lattice of posts. Physics of Fluids, 30(5), 054107.

Li, Z. Y., Xu, Y., & Wang, J. J. (2020). Similarity parameter for synthetic jet vortex rings impinging onto porous walls. AIAA Journal, 58(2), 722-732.

Lim, T. T. (1989). An experimental study of a vortex ring interacting with an inclined wall. Experiments in Fluids, 7(7), 453-463.

Lim, T. T., Nickels, T. B., & Chong, M. S. (1991). A note on the cause of rebound in the head-on collision of a vortex ring with a wall. Experiments in fluids, 12(1-2), 41-48.

Long, J., & New, T. H. (2015). A DPIV study on the effects of separation distance upon the vortical behaviour of jet–cylinder impingements. Experiments in Fluids, 56(7), 1-21.

Long, J., & New, T. H. (2019). Vortical structures and behaviour of an elliptic jet impinging upon a convex cylinder. Experimental Thermal and Fluid Science, 100, 292-310.

Mujal-Colilles, A., Dalziel, S. B., & Bateman, A. (2015). Vortex rings impinging on permeable boundaries. Physics of Fluids, 27(1), 015106.

Musta, M. N., & Krueger, P. S. (2014). Interaction of vortex rings with multiple permeable screens. Physics of Fluids, 26(11), 113101.

Naaktgeboren, C., Krueger, P. S., & Lage, J. L. (2012). Interaction of a laminar vortex ring with a thin permeable screen. Journal of fluid mechanics, 707, 260.

Naitoh, T., Banno, O., & Yamada, H. (2001). Longitudinal vortex structure in the flow field produced by a vortex ring impinging on a flat plate. Fluid Dynamics Research, 28(1), 61.

Naitoh, T., Sun, B., & Yamada, H. (1995). A vortex ring travelling across a thin circular cylinder. Fluid Dynamics Research, 15(1), 43-56.

New, T. H., & Long, J. (2015). Dynamics of laminar circular jet impingement upon convex cylinders. Physics of Fluids, 27(2), 024109.

New, T. H., Long, J., Zang, B., & Shi, S. (2020). Collision of vortex rings upon V-walls. Journal of Fluid Mechanics, 899.

New, T. H., Shi, S., & Zang, B. (2016). Some observations on vortex-ring collisions upon inclined surfaces. Experiments in Fluids, 57(6), 109.

New, T. H., & Zang, B. (2017). Head-on collisions of vortex rings upon round cylinders. Journal of Fluid Mechanics, 833, 648-676.

Nguyen, V. L., Takamure, K., & Uchiyama, T. (2019). Deformation of a vortex ring caused by its impingement on a sphere. Physics of Fluids, 31(10), 107108.

Orlandi, P., & Verzicco, R. (1993). Vortex rings impinging on walls: axisymmetric and three-dimensional simulations. Journal of Fluid Mechanics, 256, 615-646.

Patankar, S. (2018). Numerical heat transfer and fluid flow. Taylor & Francis.

Ren, H., Zhang, G., & Guan, H. (2015). Three-dimensional numerical simulation of a vortex ring impinging on a circular cylinder. Fluid Dynamics Research, 47(2), 025507.

Smagorinsky, J. (1963). General circulation experiments with the primitive equations: I. The basic experiment. Monthly Weather Review, 91(3), 99-164.

Sun, Z., & Brücker, C. (2017). Investigation of the vortex ring transition using scanning Tomo-PIV. Experiments in Fluids, 58(4), 36.

Swearingen, J. D., Crouch, J. D., & Handler, R. A. (1995). Dynamics and stability of a vortex ring impacting a solid boundary. Journal of Fluid Mechanics, 297, 1-28.

Verzicco, R., & Orlandi, P. (1994). Normal and oblique collisions of a vortex ring with a wall. Meccanica, 29(4), 383-391.

Vuorinen, V., Keskinen, J. P., Duwig, C., & Boersma, B. J. (2014). On the implementation of low-dissipative Runge–Kutta projection methods for time dependent flows using OpenFOAM®. Computers & Fluids, 93, 153-163.

Walker, J. D. A., Smith, C. R., Cerra, A. W., & Doligalski, T. L. (1987). The impact of a vortex ring on a wall. Journal of Fluid Mechanics, 181, 99-140.

Xu, Y., Li, Z. Y., Wang, J. J., & Yang, L. J. (2019). On the interaction between turbulent vortex rings of a synthetic jet and porous walls. Physics of Fluids, 31(10), 105112.

Xu, Y., Li, Z. Y., & Wang, J. J. (2021). Experimental investigation on the impingement of synthetic jet vortex rings onto a porous wall. Physics of Fluids, 33(3), 035140.